Full length article

The role of doping and microstructure on hydrogen solubility in monoclinic ZrO$_2$: Experimental validations of simulated defect chemistry

William J. Bowman*, Jing Yang, Bilge Yildiz*

Laboratory for Electrochemical Interfaces, Department of Nuclear Science and Engineering, Department of Materials Science and Engineering, Massachusetts Institute of Technology, 77 Massachusetts Avenue, Cambridge, MA 02139, USA

ARTICLE INFO

ABSTRACT

The effect of chemical doping and ceramic microstructure on H solubility was measured systematically for the first time in monoclinic ZrO$_2$. Excitingly, the influence of chemical doping by Fe, Cr and Ta cations on bulk H solubility was in qualitative agreement with defect chemistry simulations based on density functional theory and statistical thermodynamics. This is the first experimental validation of the recently-developed modeling framework, which is capable of high-throughput defect chemistry computations of light elements in metal oxides. H solubility was quantified using temperature-programmed desorption and was measured for various microstructures and under varied oxygen partial pressure, enabling us to identify the microstructural origin (i.e. bulk, surfaces and grain boundaries) of sorbed H defects and infer their defect type. Doping the oxide resulted in a significant increase in the H-uptake time, indicating that solute cations slowed H defect diffusion. Ta doping offered the lowest bulk H solubility at all measurement temperatures (410 °C–60 °C), though Fe doping also lowers bulk solubility at lower temperatures and yielded the most tightly bound H defects of all oxides. This could be significant in applications where one wishes to minimize H permeation *via* limiting diffusion kinetics. Based on this work we emphasize the role of both doping and microstructure on the overall H uptake and highlight the importance of elucidating the relative nuances of each oxide system; we thus reiterate the value of a high-throughput computational analysis.

© 2020 Acta Materialia Inc. Published by Elsevier Ltd. All rights reserved.

1. Introduction

Metal oxide ceramics and thin films are employed broadly in the science and engineering of advanced energy materials and nanotechnology. Absorption and adsorption of hydrogen, hydroxyls, and water by these materials is critical to their performance in energy conversion [1,2], harvesting [3] and storage [4–6] applications. There has been sustained interest in solid oxide cells that employ metal oxide catalysts to perform hydrogen and/or water dissociation reactions [1], or rely on solid H electrolytes [7]. Thermochemical syngas (H$_2$ and CO) production schemes using reducible metal oxides to remove oxygen from water and CO$_2$ are also under investigation [2]. Absorption of H was shown to improve conductivity without sacrificing transparency in polycrystalline ZnO, which was proposed as an alternative to Sn-doped indium oxide in Si-based solar cells [3]. Li$^+$ charge transfer across the electrolyte-electrode interface critically impacts solid state battery performance, and studies show that protonation of the solid oxide Li$^+$ electrolyte is a key reaction in the formation of Li-blocking carbonates at this interface [4,6]. The ability to reversibly hydrate VO$_2$ thin films was also demonstrated recently, motivating

their proposal as a novel H storage medium [5]. In the context of nuclear energy, water and H absorbed by UO$_2$ [8–10] has been cited as a source for H which embrittles Zr alloy cladding, whose oxide scale has also been the subject of hydration studies [11–13]. Gaining a fundamental understanding of the chemical interactions between H and metal oxides — as well as developing the ability to predict them with high-throughput computational simulations — undergirds progress in materials science and will accelerate the rational design of future materials.

The present work focuses on quantifying and elucidating H solubility in cation-doped monoclinic ZrO$_2$ (α-ZrO$_2$), which was the subject of a recent computational study by our group [13]. In that work, Youssef *et al.* developed a thermodynamic modeling framework based on density functional theory (DFT) [13–15] that predicts chemical and charge transport properties critical to H uptake in doped α-ZrO$_2$. For example, they showed that the predominant H point defects in doped α-ZrO$_2$ at 600 K are either interstitial H or a H-Zr vacancy complex, depending on the dopant species. Importantly, that work produced material design guidelines for mitigating H uptake based on (i) thermodynamically lowering the H solubility and (ii) kinetically accelerating H$_2$ evolution at the α-ZrO$_2$ surface in contact with H^+. However, a first experimental validation of this framework is absent from the literature. If validated the framework could provide high-throughput

Table 1
Oxide fabrication details.

	ZrO_2	Fe-doped	Cr-doped	Ta-doped
Nominal dopant, D, concentration (x in $D_xI_yZr_{1-x-y}O_2$)	0	$1.00 \cdot 10^{-2}$	$9.40 \cdot 10^{-3}$	$3.31 \cdot 10^{-3}$
Nominal impurity, I, concentration (y in $D_xI_yZr_{1-x-y}O_2$)	$2.2 \cdot 10^{-4}$	$2.18 \cdot 10^{-4}$	$2.65 \cdot 10^{-4}$	$2.22 \cdot 10^{-4}$
Molar mass (g mole^{-1})	123.218	122.8	122.8	123.5
Theoretical density, ρ_{Theory} (g cm^{-3})	5.68	5.66	5.66	5.69
Total density, geometric ($\pm$ 0.01 g cm^{-3})	3.27	3.83	3.57	3.43
Supplier (purity,%)	Alpha Aesar, Puratronic (99.978)	Sigma Aldrich ($\geq$ 99.995)	Sigma Aldrich (99)	Alpha Aesar (99.85)

analyses and predictions of many metal oxides, particularly those containing light-element point defects such as H and Li.

Beyond serving as a model oxide, α-ZrO$_2$ passivates Zr alloys in nuclear reactors [11,16], and has been studied for heterogeneous catalysis [17−22] and photocatalytic water splitting [23] applications. However, experimental studies quantifying H solubility in this material appear limited to undoped α-ZrO$_2$. Yamanaka *et al.* measured solubility in sintered α-ZrO$_2$ pellets hydrated between 500 − 1000 °C and showed that solubility decreases with increasing hydration temperature from $\sim$10^{-4} to $\sim$10^{-5}H/ZrO$_2$ [24]. In tetragonal ZrO$_2$, Park and Olander measured similar levels of H solubility at 1300 °C − 1600 °C [25]. We hope this work can illuminate the positive and negative impacts of various cation dopants selected based on our initial computational work mentioned above.

We also aim to elucidate the impact of microstructural features on H sorption in doped α-ZrO$_2$, where *quantitative* studies again appear to be limited to undoped α-ZrO$_2$. In sintered polycrystalline α-ZrO$_2$, Yamanaka *et al.* measured distinct H$_2$O desorption events around 150 °C and 500 °C, attributed to surface and bulk desorption, respectively [24]. Attribution of low-temperature desorption to surface-physisorbed H$_2$O was corroborated by Kouva *et al. via* desorption from α-ZrO$_2$ particles [20]; the contribution of internal surfaces and interfaces to H absorption has not been clarified. Navio *et al.* showed using IR spectroscopy that hydroxyls and molecular water adsorbed on Fe-doped ZrO$_2$ ($<$ 5 wt% Fe) nanoparticles [26]. Studies of H permeation through oxide scales of Zr alloys indicate that grain boundaries, pores, and cracks are diffusion pathways facilitating oxidative corrosion. Sundell *et al.* investigated oxide chemistry by atom probe tomography and showed that Ni, Fe^{2+} [27] and OH$^+$ [11,12] decorated grain boundaries in the corrosion scale on Zircaloy-2 and Zr-2.5Nb. However, there persists a gap in the qualitative and quantitative understanding of the effect of doping α-ZrO$_2$ on H sorption at microstructural features like pores, surfaces and grain boundaries.

In this work, we systematically investigated the effects of chemical doping and microstructure modification on H solubility in monoclinic ZrO$_2$ doped with Fe, Cr or Ta. These dopants were selected following recent theoretical predictions of composition-dependent H solubility in this oxide by Youssef *et al.* [13]. Hydrogen solubility was measured *via* temperature-programmed desorption (TPD) for various microstructures and oxygen partial pressures, which allowed us to identify the origin of H defects in the oxides (i.e. bulk, surfaces and grain boundaries). To elucidate the type of H defects, solubility was measured under varied oxygen partial pressure, accentuating the role of oxygen in the H desorption process. Our measurements demonstrate that multiple H-containing defects and complexes are formed during bulk and surface hydration. We show that chemical doping effectively modulates H solubility in monoclinic ZrO$_2$, though we emphasize the role of microstructure control in controlling H sorption in certain compositions. Measurements of bulk H solubility presented here are in qualitative agreement with updated defect chemistry simulations based on DFT, which is the first experimental validation of the framework's predictive capability and we reiterate its potential for accelerating the rational design of materials containing light-element point defects such H and Li.

2. Methods

2.1. Monoclinic ZrO$_2$ pellets were fabricated via solid state synthesis

A solid-state route was used to synthesize doped oxides pellets. ZrO$_2$ powder was mechanically mixed using a mortar and pestle with Cr$_2$O$_3$, Fe$_2$O$_3$, and Ta$_2$O$_5$ powders to yield nominally D$_x$Zr$_{1-x}$O$_2$, where D is Cr, Fe or Ta, and $x < 0.01$,

Table 1. A binder of 5 wt% polyvinyl alcohol dispersed in distilled water was ground into the powder, which was pressed to pellets under uniaxial compression at 235 MPa in a steel piston/dye assembly. Pellets were sintered in dedicated alumina crucibles in air for 20 h with heating and cooling rates of 2.5 °C/min. Sintering temperatures varied from 1125 °C − 1700 °C, as indicated in Fig. 3, producing disc fragments with edge length of 5 mm − 1 cm, e.g. Fig. 4c and Figure S2.

Phase analysis of the sintered pellets was performed using x-ray diffraction (XRD) with Cu K$_\alpha$ radiation (Panalytical X'Pert Pro). Mean grain diameter was measured after each heat treatment from SEM images using the mean lineal intercept method from $>$ 100 grains per sample.

The porosity of the pellets was also measured after each heat treatment. The total porosity, $P_{Total} = P_{Closed} + P_{Open}$, was determined from total density, ρ_{Total}, which was calculated from the total volume (total volume includes the solid and all porosity), and theoretical density, ρ_{Theory}, Eq. (1).

$$P_{Total} = 1 - \rho_{Total}/\rho_{Theory} \tag{1}$$

The closed porosity, P_{Closed}, was determined from the so-called *closed density, ρ_{Closed}*, calculated using the oxide volume measured *via* water displacement, Eq. (2). The closed density is calculated assuming that the measured volume includes only that of the solid oxide and any closed porosity.

$$P_{Closed} = 1 - \rho_{Closed}/\rho_{Theory} \tag{2}$$

Finally, the open porosity was calculated as $P_{Open} = P_{Total} - P_{Closed}$.

2.2. Defect chemistry was simulated using DTF and statistical thermodynamics

Equilibrium defect concentrations at various oxygen partial pressures and temperatures were predicted using a first-principles modeling framework. Formation energies of intrinsic defects and doping elements in monoclinic ZrO$_2$ are obtained from DFT calculations performed using the Vienna *Ab initio* Simulation Package (VASP) [28−30]. The generalized gradient approximation (GGA) with Perdew-Burke-Ernzerhof (PBE) functional is used [31,32]. We use a supercell size of 2 × 2 × 2 ZrO$_2$ conventional cells (32 formula units) for the defect calculations; energy cut-off is set to 700 eV and a 2 × 2 × 2 K-point grid is used. Additional details about the thermodynamic model and DFT defect calculations are provided elsewhere [13,33]. All possible interstitial sites, substitutional sites and valence states are considered for the dopant species. To compare with experiment, dopant concentrations were fixed at 1 atomic percent for all doped calculations in the defect equilibrium model.

2.3. Sintered oxides were hydrated by humid H_2 at elevated temperature

The oxides were hydrated at 410 °C – 760 °C by exposure to humidified 3% H_2:N_2 (Airgas), Fig. 4a. The sample temperature was measured with a K-type thermocouple positioned outside of the quartz tube which contained the sample and hydrating gas. The H_2:N_2 was bubbled at 20 sccm through 25 °C de-ionized water, producing a reducing gas with partial pressures of H_2O = 3.13 • 10^{-2} atm, H_2 = 2.91 • 10^{-2} atm, and N_2 = 9.40 • 10^{-1} atm. The pO_2 was 1 • 10^{-16} atm − 1 • 10^{-11} atm at the hydration temperatures, as measured with a yttria-stabilized zirconia Nernst cell with porous Pt electrodes and one side of the cell exposed to atmosphere, Figure S1. To freeze in the equilibrium defects formed under each hydrating condition, samples were cooled to room temperature within 5 mins by removing the quartz tube from the tube furnace and fanning the tube with room-temperature air using a motorized fan.

2.4. Hydration times were determined by electrical conductivity relaxation

Electrical conductivity relaxation measurements were performed at each hydrating temperature by monitoring the current response to 20 mV applied while switching the sample environment between dry O_2 and humid H_2, e.g. Fig. 4c. The oxides were contacted with electrodes comprised of 100 nm of sputtered Pt covered with Pt ink fired at 1000 °C for 1 h. Measurements were performed using a digital source measure unit (Keithley 2400) controlled by LabVIEW software.

2.5. H solubility was measured using temperature-programmed desorption

Following hydration, the H uptake was quantified using temperature-programmed desorption (TPD). Hydrated samples were transferred to a second tube furnace flow reactor equipped with a mass spectrometer configured to quantify the effluent composition, Fig. 4b. This reactor is described in detail in chapter two of the doctoral dissertation of Zhao [34]. Samples were dehydrated by heating at 10 °C/min from 25 °C to 1075 °C in dry synthetic air (21% O_2:Ar; Airgas ultrahigh purity) flowing at 25 sccm. The sample was in a quartz tube inside a three-zone tube furnace, and the temperature was measured locally by a K-type thermocouple located inside the reactor adjacent to the sample. The concentrations of desorbed H_2O and H_2 in the effluent gas were monitored using a quadrupole mass spectrometer (Hiden Analytical Inc., HPR20) whose gas-probing filament was located adjacent to the sample on the gas exhaust side. To prevent water condensation, the gas-handling tubes were heated to ∼ 130 °C. H solubility reported in Fig. 6b, d, f, h, was calculated by integrating over the temperature ranges containing peaks in the steam release rate vs. temperature profiles in Fig. 6a, c, e, g. The solubility values reported in Fig. 8a-b were calculated similarly from the release rate data in Fig. 5. The integration windows are tabulated in Table S3.

Calibration gasses were used to convert the raw signal, R_i, in Eq. (3), to gas mole fraction, X_i, in Eq. (4). B_i and η_i are the background signal and calibration factor for species i, respectively. The calibration factor was measured after each desorption measurement by flowing calibration gasses with identical flow rate and in concentrations comparable to those detected during experimental measurements. Calibration of H_2O was performed by bubbling the carrier gas through distilled water heated to 40 °C, and calibration of H_2 employed 5% H_2:Ar (Airgas).

$$Corrected\ signal\ of\ species\ i = \frac{R_i - B_i}{\eta_i} \quad (3)$$
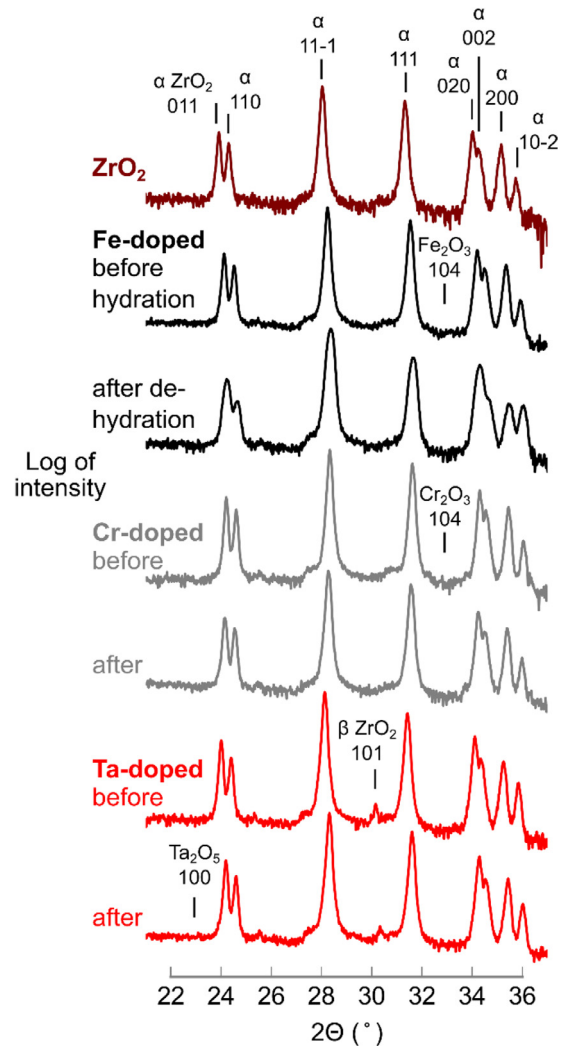

Fig. 1. X-ray diffraction revealed that the as-prepared oxides were primarily monoclinic (α) ZrO_2, and that the phase was preserved throughout (de)hydration cycling. Loci of the major reflections from the dopants' binary oxide precursors are indicated, as well as the position of the tetragonal (β) ZrO_2 {101} reflection. The only minor phase was observed in Ta-doped ZrO_2.

$$X_i = \frac{Corrected\ signal\ of\ species\ i}{\sum_j Corrected\ signal\ of\ species\ j} \quad (4)$$

3. Results & discussion

3.1. Doped monoclinic ZrO_2 pellets were fabricated with modified microstructure

The sintered ZrO_2 was monoclinic (α-ZrO_2) as confirmed by XRD, Fig. 1. The diffraction patterns were unchanged following hydration-dehydration cycling, indicating that the sintered oxides were phase stable throughout the study. Fe- and Cr-doped ZrO_2 were both monoclinic without trace of the binary precursor oxides Fe_2O_3 or Cr_2O_3. Fe is stable in α-ZrO_2 up to 15 at% [19,35]. Ruh and Garrett also showed using XRD of vacuum-sintered Cr-doped ZrO_2 that (i) Cr addition did not stabilize the tetragonal phase, (ii) Cr was lost *via* vaporization during sintering, and (iii) the Cr solubility limit was ∼ 1 at%−1.6 at% [36]. The Fe- and Cr-doped ZrO_2 were orange and blue, respectively, and the alumina crucibles in which the pellets were sintered were slightly discolored, indicating some Fe and Cr loss.

The only minor phase observed was in Ta-doped ZrO_2 ($Ta_{0.003}Zr_{0.997}O_2$), wherein a phase commonly attributed in the literature
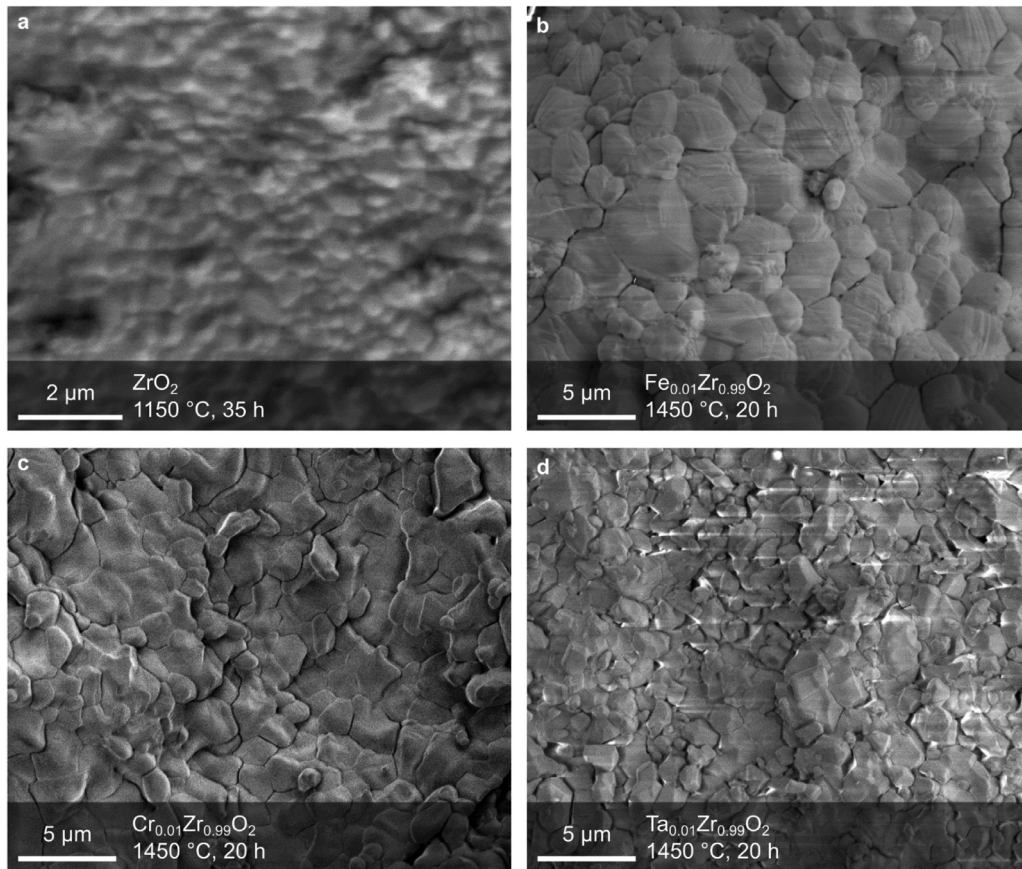
Fig. 2. Secondary electron SEM images of the as-prepared oxides with composition, sintering temperature and sintering time indicated.

to either tetragonal or orthorhombic zirconia (so-called β-ZrO$_2$) was stabilized. The Ta-doped ZrO$_2$ XRD pattern obtained before hydration (Fig. 1) was analyzed using Rietveld refinement assuming the coexistence of Ta-containing monoclinic and tetragonal phases to estimate the β-ZrO$_2$ phase fraction. This analysis indicated that the β-ZrO$_2$ phase fraction was 0.5% ± 0.2%. This is consistent with the monoclinic phase fraction expected based on a systematic study of this oxide by Sponchia *et al.* [37], though they did not investigate compositions below 1% Ta whereas we used 0.3% Ta. Bhattacharya *et al.* calculated phase diagram isothermal sections indicating that Ta$_2$O$_5$ in concentrations < 2 at% is soluble in *tetragonal* ZrO$_2$ above ∼1250 °C [38]. If we take 2 at% as the solubility limit of Ta in β-ZrO$_2$—whose phase fraction is 0.5% in our case,

then an estimated 0.01 at% of Ta dopants are stabilized in β-ZrO$_2$, leaving ∼ 0.02 at% Ta to dope the monoclinic phase.

Microstructures were evaluated throughout the study by SEM imaging, Fig. 2. The as-prepared pellets were polycrystalline with grain size 0.21 μm − 1.63 μm, Fig. 3a. Their total porosity (the sum of closed and open porosity) was 0.32−0.42, and the open porosity (the porosity connected to the pellet surface) was 0.27−0.29, Fig. 3b. Closed density (derived from the combined volume of oxide and closed pores) was 85% − 95% relative to theoretical density, indicative of a microstructure comprising regions of open porosity and a densified polycrystalline network of 85%−95% relative density. At higher sintering temperatures a decrease in closed porosity can occur if
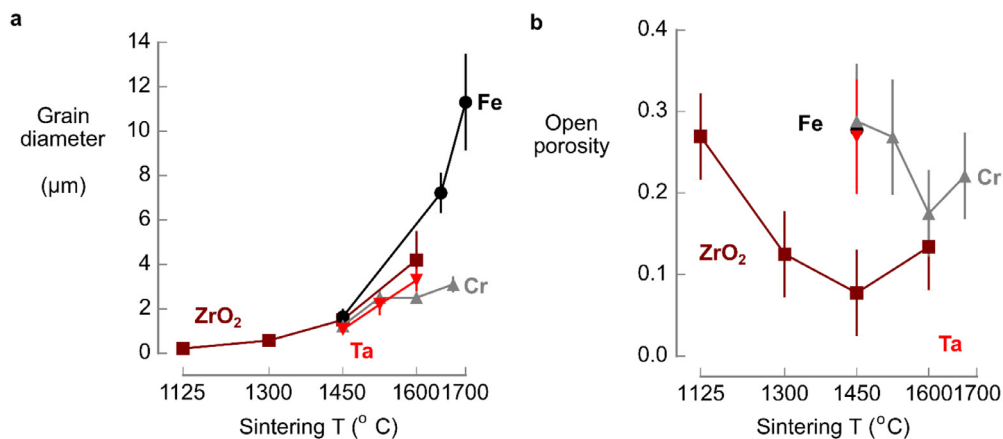

Fig. 3. Mean grain size (a) and open porosity (b) varied with increasing sintering temperature. Mean grain diameters are plotted with one standard deviation derived from measuring > 100 grains using the mean lineal intercept method. Open porosity is plotted with propagated uncertainty.

internal open pores join with the network of open porosity. This would lower the amount of closed porosity without affecting total porosity, thus increasing the measured open porosity. This is consistent with the dense polycrystalline microstructures shown in Fig. 2. The composition of the doped ZrO_2 was assumed to be uniform from grain to grain as compositional heterogeneity was not detected using SEM energy-dispersive x-ray spectroscopy or SEM backscatter imaging. The influence of grain size and open porosity on H sorption is described below.

4. H solubility was modified by doping and microstructure variation

4.1. Equilibration time under hydrating conditions was measured using electrical conductivity relaxation

To verify that the oxides reached chemical equilibrium during hydration (Fig. 4a), electrical conductivity relaxation (ECR) measurements were performed under each hydration condition, e.g. Fig. 4c. This technique detects changes in electrical conductivity during equilibration of the oxide with the hydration gas, humid 3% $H_2:N_2$ (see Methods). Ideally, a concentration gradient of the mobile defect drives mass transport in and out of the oxide, which occurs orthogonally to the measured electrical current flow. The equilibration (or *hydration*) time, therefore, is the time required for the electrical current to reach steady state after switching the gas from dry O_2 to humid H_2. Switching from dry O_2 to the hydrating gas changed the oxides' electrical conductivity, as exemplified by ZrO_2 in Fig. 4c. The time required to transition between steady states was taken as the equilibration time for hydration. For ZrO_2 at 700 °C, the conductivity

drop is attributed to a transition from p-type electronic conduction under dry O_2 (high pO_2) to oxygen ionic or n-type electronic conduction (low pO_2) in the hydration gas – whose pO_2 was $1 \cdot 10^{-16}$ atm$-1 \cdot 10^{-11}$ atm at the hydration temperatures. This would be consistent with experimental work by Kumar et al. [39] on the pO_2 dependence of electrical conductivity above 600 °C, and theoretical work of Youssef et al. [13] who computed the pO_2 dependent defect chemistry at 323 °C and 923 °C.

Hydration times decreased with increasing hydration temperature, attributed to slower diffusion kinetics at lower temperatures, Fig. 4d. Hydration times reported here for α-ZrO_2 are in good agreement with equilibration times reported for ECR experiments on α-ZrO_2, which range from 1 h – 4 h [39,40]. Repeated measurements of H solubility were also insensitive to hydration time above the equilibration times in Fig. 4d, which corroborated the ECR data. Interestingly, doping ZrO_2 increased hydration time at each temperature. One explanation for this was reported by Muta and Yamanaka, whose *ab initio* studies of monoclinic ZrO_2 showed that Cr and Fe dopants can be trap sites for diffusing H, thus lowering the mobility of H point defects [41]. Une et al. showed also that β-ZrO_2 had slower H diffusivity than α-ZrO_2, which may also contribute to the slower equilibration times of Ta-doped ZrO_2 relative to undoped $ZrO2$ [42].

Reversible color change during hydration was observed in each oxide: ZrO_2 turned from white to light grey suggesting oxygen deficiency [23,43], Fe-doped ZrO_2 changed from orange to blue-grey (Fig. 4e), Cr-doped ZrO_2 turned from dark to light teal-blue (Figure S2), and Ta-doped ZrO_2 turned from white to very light yellow. Decomposition or mechanical failure of the oxides did not result from (de) hydration, consistent with previous experimental work demonstrating chemical stability of ZrO_2 in solution with pH > 1.5 [44].
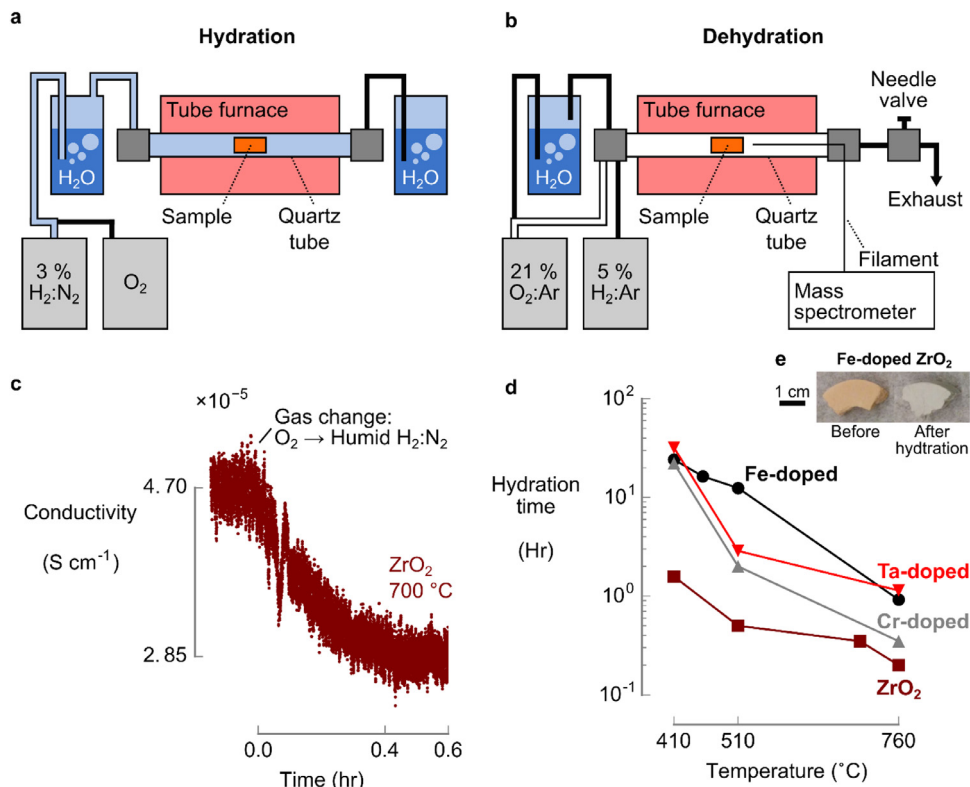

Fig. 4. Requisite hydration times were measured using electrical conductivity relaxation. (a) Oxides were hydrated at elevated temperature by exposure to humidified H_2. (b) Oxides were dehydrated by heating in dry O_2 and the effluent composition was monitored by mass spectrometry. (c) An exemplary conductivity relaxation curve shows that ZrO_2 at 700 °C equilibrates in 0.4 hours; the decrease in conductivity is attributed to a transition from p-type to oxygen ionic or n-type electronic conduction. (d) Hydration times increased with decreasing hydration temperature and upon doping ZrO_2. (e) Hydrating the oxides caused reversible color change, exemplified by pellets fragments of Fe-doped ZrO_2.

4.2. Hydrogen desorption was affected by the choice of dopant

Hydrogen desorption during dehydration was characterized using temperature-programmed desorption (TPD) measurements, where the hydrated oxides were heated in dry synthetic air (21% O_2:Ar), Fig. 4b. Water desorption was detected from all samples, and in some cases H_2 desorption was also detected. However, in those cases < 1% of the total hydrogen dissolved in the oxide was released as H_2. Multiple desorption peaks were typically observed in each desorption curve, with the curve shape varying with oxide composition and hydration temperature. Sherman and Olander compared H release from single and polycrystalline UO_2, and showed that H_2 desorption from single crystals could be described quantitatively based on H chemical diffusivity, whereas desorption curves from polycrystalline samples exhibited multiple peaks and followed no simple diffusion mechanism [9]. In that and an earlier work [8] they reported desorption peaks with sharp onsets and very clear high-temperature tails/shoulders, somewhat similar to peak shapes presented here.

The shape of water desorption profiles from ZrO_2 ('ZrO_2' in Fig. 5) was in very good agreement with data reported previously for monoclinic ZrO_2 pellets by Yamanaka et al. [24]. The desorption curves exhibit a low-temperature peak at $\sim$ 150 °C and high-temperature peak/tail at $\sim$ 550 °C, and the relative intensity of the two peaks is also in good agreement. The low-temperature desorption was observed previously by Yamanaka et al. who attributed it to desorption of surface-adsorbed water [24]. Interestingly, those desorption measurements of sintered pellets of monoclinic ZrO_2 were performed in a vacuum of 10^{-7} Pa, whereas similar studies of single crystals of tetragonal ZrO_2 by Park and Olander [25] did not detect low-temperature H

desorption from samples measured in a vacuum furnace (no base pressure was reported). This suggests that surface defects present in polycrystalline ZrO_2 plays a critical role in the adsorption of H-containing species. The high-temperature desorption increased with decreasing hydration temperature, which is again in fair agreement with the report of Yamanaka et al., as discussed below.

Kouva et al. [20] investigated water's interaction with the surface of monoclinic ZrO_2 particles (240 μm $-$ 500 μm) using a combination of TPD and optical spectroscopy. Water desorption from their reduced/hydrated sample in N_2 began around 150 °C and peaked around 250 °C $-$ 300 °C, with a tailing decay in desorption to over 550 °C. In addition to TPD, the authors correlated sample temperature during desorption with diffuse reflectance infrared Fourier transform spectroscopy (DRIFTS) to characterize the surface-related H species during heating. When heating the reduced/hydrated ZrO_2 in N_2 they showed that the predominant form of chemisorbed H was in hydroxyl groups with O multi-coordinated with lattice Zr. The combination of their desorption measurement—which is in qualitative agreement with our observations of ZrO_2—and their DRIFTS result assists in our attribution of low-temperature water desorption to a combination of (i) physisorbed water and (ii) chemisorbed hydroxyl groups which are multi-coordinated likely by filling O vacancies formed in the reducing environment present during hydration. Additionally, the coexistence of multiple 'liquid-like' and 'ice-like' surface-adsorbed waters on porous Y-stabilized tetragonal ZrO_2 at low temperatures was established experimentally by Stub et al. [45].

For Cr-doped ZrO_2 two distinct water desorption processes were observed, with the high-temperature desorption increasing with decreasing hydration temperature. The release rate from Fe-doped
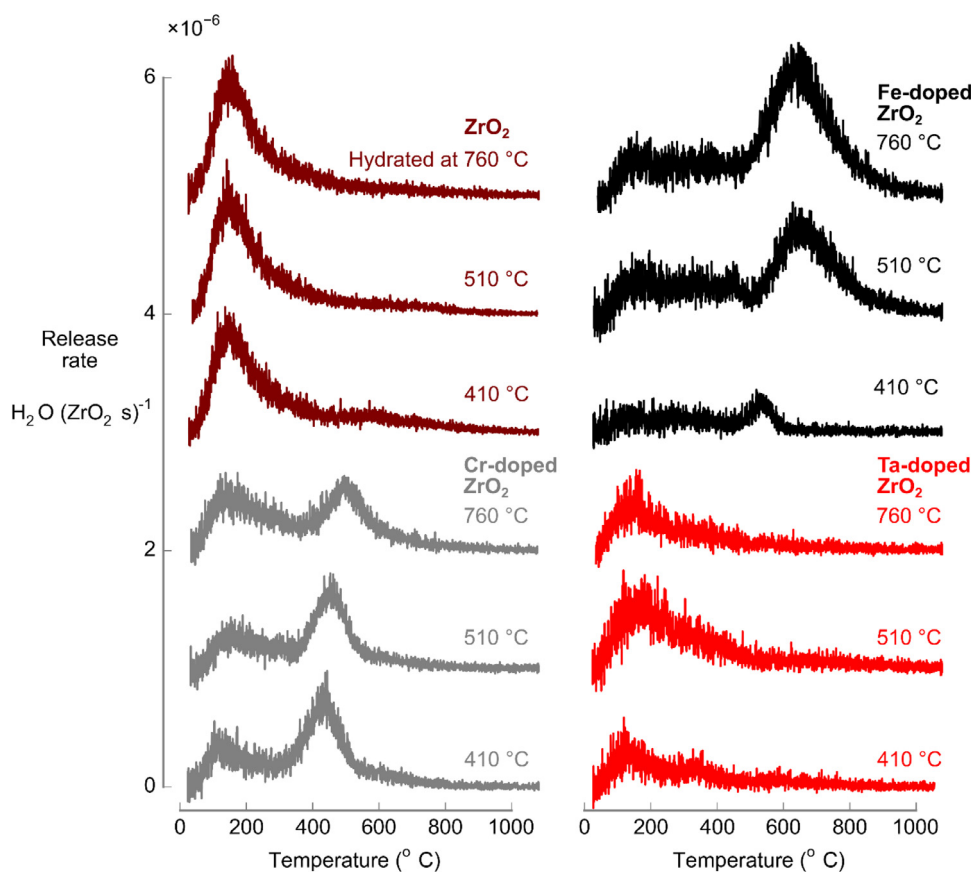

Fig. 5. Water release was measured from hydrated monoclinic ZrO_2 oxides using temperature-programmed desorption. The release rate of water molecules per unit cell of ZrO_2 per second was measured by mass spectrometry as the oxides were heated from 25 °C to 1100 °C in dry air. The dopant species and hydration temperatures are indicated for each set of color-coded curves. Quantitative comparison of these curves is given in Fig. 8a-b, which presents the H solubility values derived from integration of the low- and high-temperature release rate peaks. The profiles are offset to ease comparison of the profile shapes.

ZrO_2 increased modestly at low temperature and was sustained at that initial level until ~ 450 °C, when desorption increased rapidly to its peak value before decaying to the baseline value at 1000 °C. Unlike the undoped case, the high-temperature desorption process decreased with decreasing hydration temperature. Ta-doped ZrO_2 performed similarly to undoped ZrO_2 in terms of water release rate, though its low-temperature desorption peaks were less intense. The subsequent sections of this paper elucidate the H-containing defects from which the desorbed H originate and quantify H solubility from desorption data in Fig. 5. The impact/role of each dopant on stabilizing sorbed H is examined and discussed throughout the subsequent sections.

4.3. Microstructure variations influenced H absorption

To assist interpretation of the desorption profiles in Fig. 5 we varied the oxides' grain size and porosity *via* heat treatments, which impacts the concentration of H binding sites such as surfaces and grain boundaries without changing the number of bulk sites. Increasing the annealing temperature increased the mean grain size (measured from SEM images, Figure S3 – Figure S6) and decreased the open porosity, Fig. 3.

In ZrO_2 increasing the annealing temperature from 1125 °C to 1600 °C increased the grain size from 0.21 μm to 4.2 μm and decreased the open porosity from 0.27 to ~ 0.1, Fig. 3. The water desorption profiles from samples annealed at higher temperatures, e. g. 1600 °C, contain two peaks, Fig. 6a. The low-temperature peak (*Peak 1*) generally decreased with annealing temperature, while the high higher-temperature peak (*Peak 2*) was insensitive to annealing temperature. In this sample Peak 1 is attributed to desorption of surface-adsorbed water (see also Fig. 7), suggesting that pore shrinkage may explain the decreased desorption with annealing. Because Peak 2 in this sample is insensitive to annealing temperature it is attributed to bulk defects, discussed below (Fig. 7). When varying sintering temperature, the hydration temperature was fixed at 760 °C.

For Fe-doped ZrO_2, increasing the annealing temperature resulted in grain growth from 1.63 μm to 11.3 μm, Fig. 3a. This grain growth was accompanied by a slight reduction of the closed density, indicating that closed porosity increased with sintering temperature. The open porosity was not measured, however, because reliable dry density measurements could not be performed; increasing the sintering temperature from 1450 °C to 1650 °C, and then to 1700 °C caused disintegration of the pellet fragments into small, ill-defined pieces < 3 mm whose dry volume could not be reliably determined.

Increasing the annealing temperature revealed three unique water desorption peaks in Fe-doped ZrO_2, whose relative intensities and positions varied considerably with sintering, Fig. 6c. Desorption in peak 1 (below 250 °C, colored blue) was found to decrease slightly with increasing sintering temperature, with H solubility dropping from $1.70 \cdot 10^{-4}$ to $5.92 \cdot 10^{-5}$ H/ZrO_2 attributed to desorption of physisorbed water molecules, Fig. 6d. This was concluded based first on the expectation that open porosity decreased slightly *via* densification during sintering—which should reduce the surface area, and second on desorption measurements performed under O_2-poor conditions, Fig. 7.

Water desorption in peak 2 showed no obvious trend with annealing temperature, and H solubility was constant at $\sim 3 \cdot 10^{-4}$ H/ZrO_2. Unlike peak 1, desorption in peak 2 *did* consume O_2 under O_2-poor conditions (Fig. 7), suggesting that the H-containing desorbing species may be surface hydroxyls or protons. It is unclear whether these are bound to the oxide surface or absorbed at grain boundaries. Though, considering the insensitivity of peak 2 to changes in grain boundary area, it may be reasonable to assume these species are not related to grain boundaries. Peak 2 also appears to shift to higher desorption temperatures, which may indicate that the desorbing species adhere more strongly to the oxide surface which has experienced higher sintering temperatures.

Water desorption in peak 3 was the most sensitive to sintering, with H solubility decreasing from $1.14 \cdot 10^{-3}$ to $8.16 \cdot 10^{-5}$ H/ZrO_2. This approximately 14-fold decrease in peak 3 H desorption corresponded to an increase in grain diameter from ~ 2 μm to ~ 12 μm. This peak is tentatively attributed to the desorption of H absorbed at grain boundaries. The ratio of grain boundary area (i.e. the area of a grain's surface) to grain volume has an inverse dependence on grain diameter, so an increase in the grain diameter by six times should correspond to an equal drop in the grain boundary area. Assuming the grain boundary H coverage does not change during sintering, the decrease of 14 times is a factor of two greater than expected, so we suspect that the grain boundary areal coverage decreases during sintering. It is likely that the local defect concentrations at grain boundaries following heating to 1450 °C varies from the defect concentrations following sintering at 1650 °C. It is well known that solutes and impurities accumulate at oxide grain boundaries which may serve to decrease the H coverage, in this case by a factor of about two. It was shown experimentally that Fe^{3+} segregation as $Fe^{/}_{Zr}$ to the surface of Fe-doped ZrO_2 lowered the oxide's catalytic activity by reducing the capacity of the surface to accommodate OH^- groups [46]. In our case, accumulated $Fe^{/}_{Zr}$ may be lower the H capacity of grain boundaries in a similar manner. The Fe-doped sample crumbled into ~ 3 mm fragments after repeated heat treatments. This was observed previously by Beck and Kaliba, who state that Fe is incorporated into ZrO_2 in the +3 oxidation state, but at high temperature changes to +2 leading to more oxygen vacancies in the tetragonal lattice and thus greater lattice parameter mismatch with the monoclinic phase which exacerbates stress [35].

For Cr-doped ZrO_2, increasing the annealing temperature from 1450 °C to 1675 °C yielded modest grain growth and open pore shrinkage, from 1.24 μm to 3.1 μm and from 0.29 to 0.22, respectively, Fig. 3. This relatively small influence of annealing temperature on grain size compared to the Fe-doped case may be related to Cr loss from the solid solution during annealing. Following each heat treatment, the color of the alumina sample crucible was changed to scarlet, with the intensity of scarlet coloration increasing with annealing temperature. Ruh and Garrett showed using XRD of vacuum-sintered Cr-doped ZrO_2 that Cr was lost *via* vaporization during sintering [36]. Here, since grain growth was minimal, it seems that the high mobility of the Cr ions served primarily to deplete the oxide of Cr *via* diffusion into the alumina crucible rather than to promote sintering.

The water desorption profiles from Cr-doped ZrO_2 had two distinct peaks: Peak 1 from 40 °C – 350 °C, and Peak 2 from 350 °C – 1000 °C, Fig. 6e. The amount of H desorption in low-temperature Peak 1 decreased with increasing annealing temperature (Fig. 6f), likely reflecting the drop in the surface area associated with open porosity. Like previous cases Peak 1 was attributed to desorption of water physisorbed to surfaces based both on the temperature range and O_2-poor desorption measurements presented below, Fig. 7. The amount of H in Peak 2 did not vary significantly with annealing temperature, suggesting that these H may originate from bulk defects rather than defects associated with grain boundaries. According to our simulations of formation free energies detailed in [13] and presented here, we believe H stabilizes as interstitial defects in Cr-doped ZrO_2 at the hydration temperatures use here. This is consistent with the experimental observation that the desorbing H originates from bulk defect in this oxide. From O_2-poor measurements, Peak 2 desorption was accompanied by a very aggressive O_2 consumption, indicative of desorption of H in the form of hydroxyls or protons; the latter interpretation being consistent with our belief that H exists as interstitials.

For Ta-doped ZrO_2, the surface desorption peak (Peak 1) unexpectedly increased despite the oxide sintering during serial annealing. Accumulation of Ta on the surface of Ta-doped ZrO2 was shown to increase the catalytic activity for 2-propanol dehydration [47], so perhaps segregation of Ta as $Ta^{\cdot}_{Zr}$ during sintering increases surface
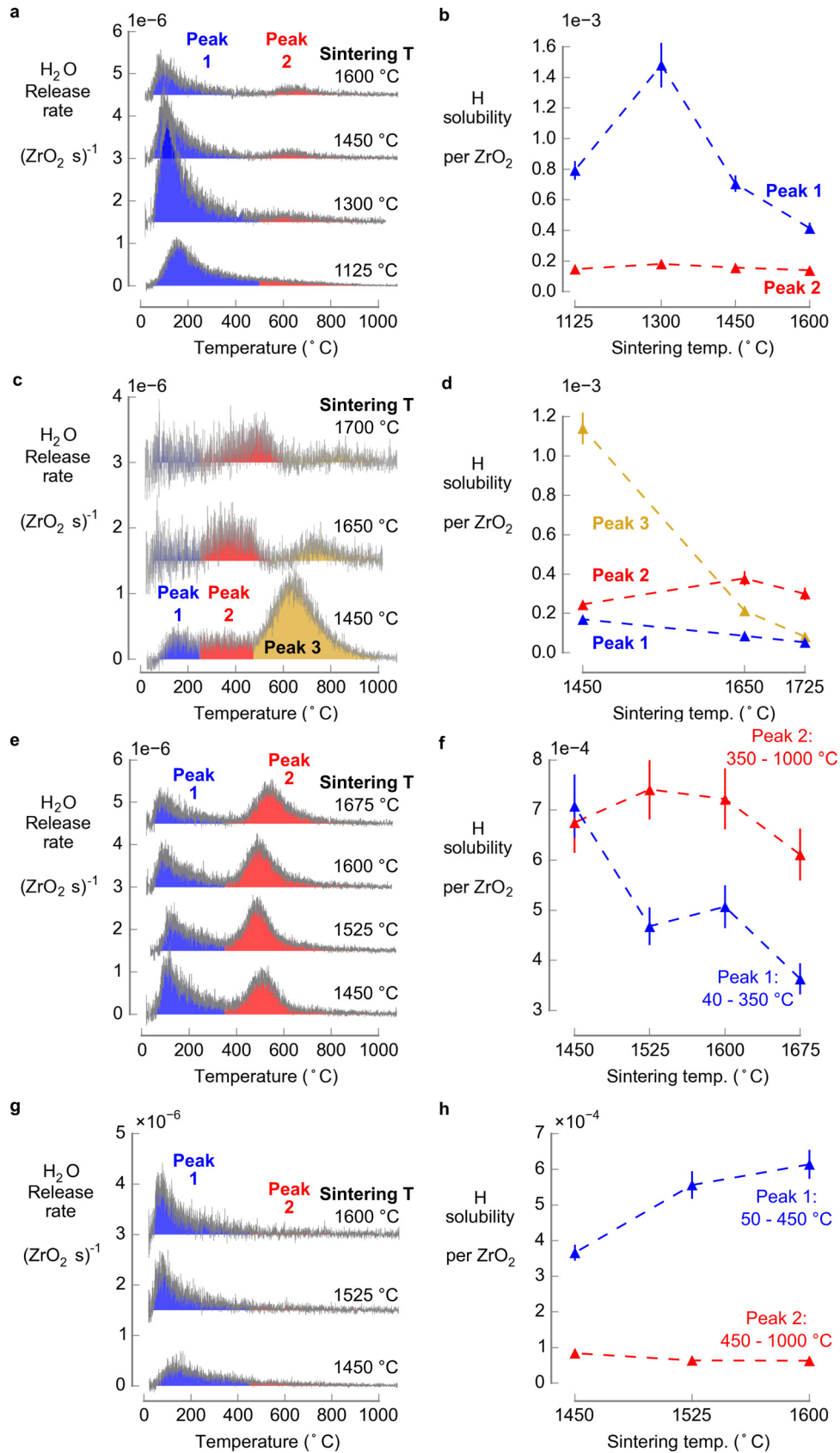
Fig. 6. Desorption measurements were performed as a function of annealing/sintering temperature, which affected the oxides' porosity and grain size. (a,b) ZrO_2, (c,d) Fe-doped ZrO_2, (e,f) Cr-doped ZrO_2, (g,h) Ta-doped ZrO_2. (a,c,e,g) The steam release rate (H_2O per unit cell of ZrO_2 per second) from each ZrO_2-based material after sequential heat treatments at various sintering temperatures. Samples were hydrated at 760 °C and water release rates were measured by temperature-programmed desorption. Multiple water desorption peaks (numbered 1, 2 or 3) were observed during TPD measurements. (b,d,f,h) H solubility associated with each of the desorption peaks was quantified as a function of sintering temperature. The profiles are offset to ease comparison of the profile shapes.
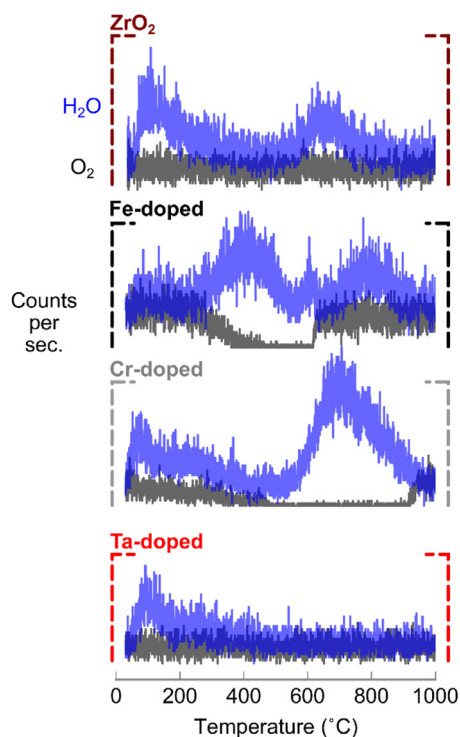
Fig. 7. Desorption measurements were performed under O_2-poor conditions (i.e. in inert carrier gas N_2 or Ar) to elucidate the origin of the desorbing H. Uncalibrated H_2O (blue) and O_2 (black) mass spectrometer signals are presented for ZrO_2 annealed at 1600 °C, Fe-doped ZrO_2 annealed at 1650 °C, Cr-doped ZrO_2 annealed at 1675 °C, and Ta-doped ZrO_2 annealed at 1525 °C. H_2 desorption was not detected, so the signal is omitted for clarity.

reactivity with OH^- groups, promoting hydration/hydroxylation. This could explain why surface desorption increased with annealing temperature. Perhaps Ta surface segregation during sintering gives rise to more surface adsorption *via* hydride or hydroxide formation, though further study is required to be conclusive. Like the other oxides, Peak 2 desorption was basically insensitive to annealing which indicates that it may be attributable to bulk H defects.

5. Desorbed H species were investigated *via* oxygen-poor TPD

To elucidate the type of H-containing species desorbing during TPD, measurements were performed using an inert carrier gas (Ar or N_2), rather than synthetic air, Fig. 7. Use of inert carrier gas significantly lowered the pO_2 during desorption, which accentuated the effect of O_2 on desorption processes. (A detectable amount of O_2 was present in the reactor presumably due to imperfect sealing.) In all cases H_2 desorption was negligible. As above, during heating of ZrO_2 two primary water desorption processes occurred both without O_2 consumption. It has been established above that the low-temperature desorption results from desorption of molecular water from surfaces, but it is remarkable that no O_2 is consumed during high-temperature water desorption. One possibility is that during hydroxyl desorption from hydrated ZrO_2, the oxide becomes oxygen-deficient (*via* reduction of the Zr cation) and lattice O is consumed to produce water. Surprisingly, O_2 is apparently not consumed to refill anion vacancies in the ZrO_2 lattice, which is known to occur during interaction of gas-phase O_2 with the oxide at high temperature.

For Fe-doped ZrO_2 desorption below 250 °C occurred without O_2 consumption, likely due to the desorption of physisorbed water. From 250 °C−625 °C water desorption occurs in conjunction with a decrease in the O_2 concentration, indicating that the desorbed H species are hydroxyls and/or protons. Interestingly, high-temperature water desorption (whose intensity decreases with increasing grain

diameter) does not consume O_2, indicating that H desorbing from grain boundaries may be consuming lattice O to form water leaving behind O vacancies.

In the Cr-doped case, water desorption below ∼ 200 °C occurred without O_2 consumption, consistent with desorption of physisorbed water. As the temperature increased to ∼ 500 °C, the O_2 signal drops gradually while the water signal remains above the baseline. This indicates desorption of H from hydroxyl or proton defects believed to be associated with microstructural features such as internal surfaces and/or interfaces; hydroxyls or protons bonded to the material's internal surfaces and/or interfaces desorb and contribute to the detected steam *via* consumption of O_2, which drops gradually in the temperature range 200−500 °C. Water desorption in this temperature range was shown to be sintering temperature dependent, Fig. 6f. At ∼ 550 °C, there is the expected intense water desorption during which the O_2 is zero, again indicating desorption of hydroxyl/protonic defects. These defects are suspected to be bulk defects since this desorption event was found to be unaffected by microstructural changes induced by annealing, Fig. 6f.

For Ta-doped ZrO_2, the O_2-poor desorption measurements looked much like the O_2-rich measurements (Fig. 6g), and there was no indication of increased O_2 consumption during water desorption. Like ZrO_2, this may simply reflect the low concentration of H defects in this oxide and thus the small amount of desorbing water, whose requisite O could be derived from non-stoichiometry created in the oxide lattice rather than the surrounding O_2 gas.

6. Solubility was measured from desorption profiles and compared with theory

With a better understanding of the origin of H defects producing the measured water desorption profiles, it was possible to determine heats of solution of H associated with surface and bulk desorption. By integrating the water desorption curves in Fig. 5 over the appropriate temperature ranges (determined from annealing-temperature-dependent desorption measurements, Table S3), we quantified H desorption attributed to (low-temperature) surface adsorption, and H desorbed at higher temperatures attributed to bulk and grain boundary (in Fe-doped ZrO_2) defects, Fig. 8. Surface-desorbed H (Fig. 8a) and high-temperature-desorbed H (Fig. 8b) were taken as unique measures of H solubility, and were fit to Eq. (5) to determine heats of solution for these H defects in the oxides [9], Table 2. Eq. (5) describes the Arrhenius relationship between H solubility, S, and the heat of solution, $h_{Solution}$, over a range of hydration temperatures, $T_{Hydration}$. A is a pre-exponential factor. The measured H solubility derived from low- and high-temperature steam desorption data (Fig. 8a-b) were plotted in the Arrhenius fashion and Eq. (5) was fit to the data using a least-squares fitting routine implemented in Python. Surface desorption increased with hydration temperature for all samples and was more endothermic when the ZrO_2 was doped, Fig. 8a and Figure S7. The low-temperature desorption of physisorbed water was reduced in all cases by doping (aside from Fe-doped ZrO_2 hydrated at 760 °C), and the lower heats of solution indicate that dopants influence surface chemical properties of the oxide *via* surface segregation during sintering. Perhaps O vacancies that serve as hydroxyl binding sites may be charge-neutralized by a segregated cation making the O site inactive for H absorption.

$$S = A \cdot exp\left(\frac{h_{Solution}}{RT_{Hydration}}\right) \tag{5}$$

The H desorbed at higher temperature was attributed to bulk and grain boundary defects, Fig. 8b and Figure S7. Like the surface, bulk and grain boundary H defects were more endothermic when the ZrO_2 was doped, Table 2. Bulk H solubility in undoped ZrO_2 increased with decreasing hydration temperature, which is in fair quantitative agreement with Yamanaka *et al.* [24] who showed that H absorption
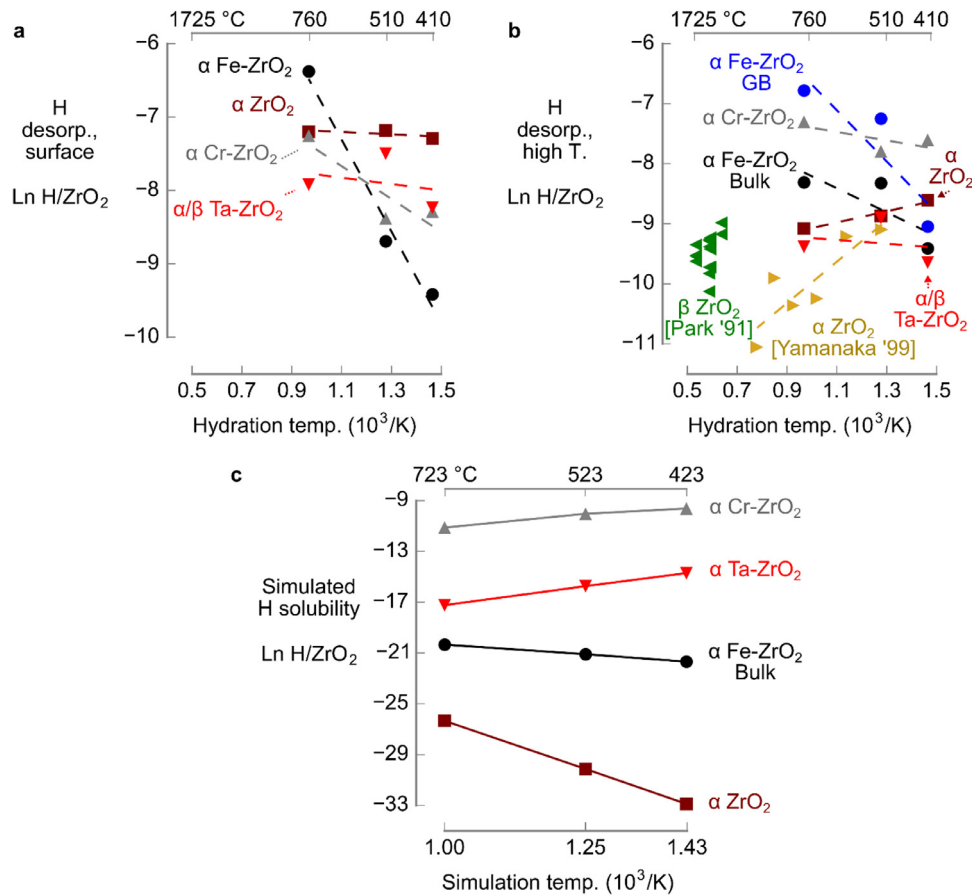
Fig. 8. Temperature programmed desorption was used to measure H desorbed from undoped and doped zirconia. (a) Surface-adsorbed H desorbed below ~ 200 °C, Fig. 5, with heats of solution indicating endothermic adsorption, Table 2. (b) Desorption from undoped, Fe- and Cr-doped monoclinic (α) zirconia, as well as Ta-doped monoclinic zirconia with 0.5% β phase fraction are in fairly good agreement with published data [24,25]. Data were fit using Eq. (5) to determine heats of solution for H, Table 2. Desorption measurements of Fe- and Ta-doped ZrO$_2$ hydrated at 410 °C were performed thrice and twice, respectively; measurements of Cr-doped ZrO$_2$ hydrated at 760 °C were performed twice. The propagated error for individual solubility measurements is approximately 5%. For solubility measurements that were repeated, the single standard deviations in these cases produce error bars smaller than the marker size.

in ZrO$_2$ is exothermic. Relative to the undoped case, Cr doping increased bulk H solubility by several times. Fe-doped ZrO$_2$ was the only material with grain boundary solubility, which decreased rapidly with decreasing hydration temperature. Sundell *et al.* used atom probe tomography to show that Fe and Ni decorate grain boundaries in oxide scale on corroded Zr alloys [27], and that OH$^+$/OD$^+$ and Fe^{2+} also accumulated at grain boundaries in these oxides [11,12]. Based on the present work, it appears that Fe doping yields the most tightly bound H defects in the bulk and at grain boundaries, which could improve the H resistance of a coating *via* kinetically limiting H diffusion. Furthermore, it seems that lower-temperature applications demanding low H solubility may benefit from Fe doping, wherein the potential for H solubility minimization appears to be most significant. In Ta-doped ZrO$_2$ the bulk H solubility was lower than the undoped case, and solubility decreased with decreasing temperature making this dopant another candidate for minimizing H solubility at low temperatures. Moreover, the absence of grain boundary H absorption may be useful when considering future microstructural optimization.

Excitingly, bulk H solubility measurements are in qualitative agreement with our theoretical predictions in several notable cases, Fig. 8c. Using a DFT-based modeling framework developed and demonstrated recently by our group [13−15], we calculated the H point defect concentration under simulated hydration conditions closely replicating those used in our experiments, see Methods and Supporting Information. There is a considerable discrepancy between the absolute values of measured and simulated solubility, perhaps suggesting the presence of additional bulk H point defects in the materials which were not in the defect chemical computation. We provide additional details discussing possible origins of these discrepancies in the Supporting Information. Our simulations indicate that bulk H solubility increases upon doping, with the trend in isothermal solubility following: Undoped < Fe-doped < Ta-doped < Cr-doped ZrO$_2$. Ignoring the Ta-doped case this trend is nearly identical to that observed in our experimental measurements, although ZrO$_2$ did absorb more H than Fe-doped ZrO$_2$ hydrated at 410 °C. While further investigation is warranted to theoretically elucidate the role of Ta doping, this

Table 2

Heats of solution for surface-desorbed H (low-temperature peak, below ~ 350 °C) and H desorbed at higher temperature (high-temperature peaks, above ~ 350 °C). *Data from [24] was fit using Eq. (5).

	α ZrO$_2$*	α ZrO$_2$ (This work)	Cr-doped α ZrO$_2$	Fe-doped α ZrO$_2$	Ta-doped α/β ZrO$_2$
Heat of solution, surface desorbed H (kJ mol^{-1})		1.3	19	52	3.6
Heat of solution, Bulk desorbed H (kJ mol^{-1})	−29	−7.7	5.9	17	2.6
Heat of solution, Grain boundary desorbed H (kJ mol^{-1})				35	

result is encouraging and highlights the predictive capability of this defect chemical modeling framework.

7. Conclusions

We performed novel systematic measurements of the effect of chemical doping and microstructure on H solubility in monoclinic ZrO_2 ceramics. Temperature-programmed desorption was used to quantify H absorption, which was measured systematically for various microstructures and under varied oxygen partial pressure conditions. This helped identify the microstructural origin of the H defects (i.e. bulk, surfaces and grain boundaries), and infer the defect type. Upon doping there was a significant increase in measured hydration times, demonstrating that solute cations slowed the diffusion of H defects in the oxides. Doping with Ta offers the lowest H solubility at all hydration temperatures (410 °C−760 °C), though Fe-doping also reduces H solubility at lower temperatures and results in the strongest H binding of all oxides, which could improve H resistance based on diffusion kinetics. While it is clear from this work that doping significantly impacts H solubility in monoclinic ZrO_2, we emphasize the role of microstructural features in controlling H sorption in these ceramics. Excitingly, the impact of chemical doping by Fe, Cr and Ta substitutional cations on bulk H solubility was found to be in qualitative agreement with our theoretical predictions made using a thermodynamic modeling framework based on DFT. This is the first experimental validation of the framework, which offers high-throughput defect chemistry simulations of metal oxides with light element point defects (e.g. H in Al_2O_3 [15]), such as advanced energy materials.

Declaration of Competing interests

The authors declare that they have no known competing financial interests or personal relationships that could have appeared to influence the work reported in this paper.

Acknowledgements

Supplementary materials

Supplementary material associated with this article can be found, in the online version, at doi:10.1016/j.actamat.2020.04.020.

References

[1] J. Myung, D. Neagu, D.N. Miller, J.T.S. Irvine, Switching on Electrocatalytic Activity in Solid Oxide Cells, Nature 537 (7621) (2016) 528 https://doi.org/10.1038/nature19090 .

[2] A.H. Bork, E. Povoden−Karadeniz, J.L.M. Rupp, Modeling thermochemical solar-to-fuel conversion: CALPHAD for thermodynamic assessment studies of perovskites, exemplified for (La,Sr)MnO3, Adv. Energy Mater. 7 (1) (2017) 1601086 https://doi.org/10.1002/aenm.201601086 .

[3] L. Ding, S. Nicolay, J. Steinhauser, U. Kroll, C. Ballif, Relaxing the conductivity/transparency trade-Off in MOCVD ZnO thin films by hydrogen plasma, Adv. Funct. Mater. 23 (41) (2013) 5177–5182 https://doi.org/10.1002/adfm.201203541 .

[4] L. Cheng, C.H. Wu, A. Jarry, W. Chen, Y. Ye, J. Zhu, R. Kostecki, K. Persson, J. Guo, M. Salmeron, G. Chen, M. Doeff, Interrelationships among Grain Size, surface composition, air stability, and interfacial resistance of Al-substituted Li7La3Zr2O12 solid electrolytes, ACS Appl. Mater. Interfaces 7 (32) (2015) 17649–17655 https://doi.org/10.1021/acsami.5b02528 .

[5] H. Yoon, M. Choi, T.-.W. Lim, H. Kwon, K. Ihm, J.K. Kim, S.-.Y. Choi, J. Son, Reversible phase modulation and hydrogen storage in multivalent VO2 epitaxial thin films, Nat. Mater. 15 (10) (2016) 1113–1119 https://doi.org/10.1038/nmat4692 .

[6] A. Sharafi, S. Yu, M. Naguib, M. Lee, C. Ma, H.M. Meyer, J. Nanda, M. Chi, D.J. Siegel, J. Sakamoto, Impact of air exposure and surface chemistry on Li−Li7La3Zr2O12 interfacial resistance, J. Mater. Chem. A 5 (26) (2017) 13475–13487 https://doi.org/10.1039/C7TA03162A .

[7] H. Iwahara, T. Esaka, H. Uchida, N. Maeda, Proton conduction in sintered oxides and its application to steam electrolysis for hydrogen production, Solid State Ion 3 (1981) 359–363.

[8] D.R. Olander, D. Sherman, M. Balooch, Retention and release of water by sintered uranium dioxide, J. Nucl. Mater. 107 (1) (1982) 31–45 https://doi.org/10.1016/0022-3115(82)90556-6 .

[9] D.F. Sherman, D.R. Olander, Hydrogen dissolution in and release from nonmetals: I. uranium dioxide, J. Nucl. Mater. 166 (3) (1989) 307–320 https://doi.org/10.1016/0022-3115(89)90227-4 .

[10] J.M. Flitcroft, M. Molinari, N.A. Brincat, N.R. Williams, M.T. Storr, G.C. Allen, S.C. Parker, The critical role of hydrogen on the stability of oxy-hydroxyl defect clusters in uranium oxide, J. Mater. Chem. A 6 (24) (2018) 11362–11369 https://doi.org/10.1039/C8TA02817F .

[11] G. Sundell, M. Thuvander, A.K. Yatim, H. Nordin, H.-.O. Andrén, Direct observation of hydrogen and deuterium in oxide grain boundaries in corroded zirconium alloys, Corros. Sci. 90 (2015) 1–4 https://doi.org/10.1016/j.corsci.2014.10.016 .

[12] G. Sundell, M. Thuvander, H.-.O. Andrén, Barrier oxide chemistry and hydrogen pick-up mechanisms in zirconium alloys, Corros. Sci. 102 (2016) 490–502 https://doi.org/10.1016/j.corsci.2015.11.002 .

[13] M. Youssef, M. Yang, B. Yildiz, Doping in the valley of hydrogen solubility: a route to designing hydrogen-resistant zirconium alloys, Phys. Rev. Appl. 5 (1) (2016) https://doi.org/10.1103/PhysRevApplied.5.014008 .

[14] J. Yang, M. Youssef, B. Yildiz, Oxygen self-diffusion mechanisms in monoclinic Zr O 2 revealed and quantified by density functional theory, random walk analysis, and kinetic Monte Carlo calculations, Phys. Rev. B 97 (2) (2018) https://doi.org/10.1103/PhysRevB.97.024114 .

[15] V. Somjit, B Yildiz, Doping α-Al2O3 to reduce its hydrogen permeability: thermodynamic assessment of hydrogen defects and solubility from first principles, Acta Mater 169 (2019) 172–183 https://doi.org/10.1016/j.actamat.2019.02.031 .

[16] N. Vermaak, G. Parry, R. Estevez, Y. Bréchet, New insight into crack formation during corrosion of zirconium-based metal-oxide systems, Acta Mater 61 (12) (2013) 4374–4383 https://doi.org/10.1016/j.actamat.2013.04.009 .

[17] T. Onishi, H. Abe, K. Maruya, K.I.R. Domen, Spectra of hydrogen adsorbed on ZrO2, J. Chem. Soc. Chem. Commun. 9 (1985) 617–618.

[18] D. Eder, R. Kramer, The stoichiometry of hydrogen reduced zirconia and its influence on catalytic activity, Phys. Chem. Chem. Phys. 4 (5) (2002) 795–801 https://doi.org/10.1039/B109887J .

[19] G. Herrera, N. Montoya, A. Doménech-Carbó, J.S. Alarcón, Characterization and electrochemical properties of iron-zirconia solid solution nanoparticles prepared using a sol−gel technique, Phys. Chem. Chem. Phys. 15 (44) (2013) 19312 https://doi.org/10.1039/c3cp53216j .

[20] S. Kouva, J. Andersin, K. Honkala, J. Lehtonen, L. Lefferts, J. Kanervo, Water and carbon oxides on monoclinic zirconia: experimental and computational insights, Phys. Chem. Chem. Phys. 16 (38) (2014) 20650–20664 https://doi.org/10.1039/C4CP02742F .

[21] A. Ruiz Puigdollers, S. Tosoni, G. Pacchioni, Turning a nonreducible into a reducible oxide via nanostructuring: opposite behavior of bulk ZrO2 and ZrO2 nanoparticles toward H2 adsorption, J. Phys. Chem. C 120 (28) (2016) 15329–15337 https://doi.org/10.1021/acs.jpcc.6b05984 .

[22] T. Otroshchenko, O. Bulavchenko, H.V. Thanh, J. Rabeah, U. Bentrup, A. Matvienko, U. Rodemerck, B. Paul, R. Kraehnert, D. Linke, E.V. Kondratenko, Controlling activity and selectivity of bare zro2 in non-oxidative propane dehydrogenation, Appl. Catal. Gen. 585 (2019) 117189 https://doi.org/10.1016/j.apcata.2019.117189 .

[23] A. Sinhamahapatra, J.-.P. Jeon, J. Kang, B. Han, J.-.S. Yu, Oxygen-deficient zirconia (ZrO2−x): a new material for solar light absorption, Sci. Rep. 6 (1) (2016) https://doi.org/10.1038/srep27218 .

[24] S. Yamanaka, T. Nishizaki, M. Uno, M. Katsura, Hydrogen dissolution into zirconium oxide, J. Alloys Compd 293−295 (1999) 38–41 https://doi.org/10.1016/S0925-8388(99)00396-5 .

[25] K. Park, D.R. Olander, Hydrogen dissolution in and release from nonmetals: III, tetragonal zirconia, J. Am. Ceram. Soc. 74 (1) (1991) 72–77.

[26] Hidalgo Navío, G. Colón, S.G. Botta, M.I. Litter, Preparation and physicochemical properties of ZrO 2 and Fe/ZrO 2 prepared by a Sol−Gel technique, Langmuir 17 (1) (2001) 202–210 https://doi.org/10.1021/la000897d .

[27] G. Sundell, M. Thuvander, H.-.O. Andrén, Enrichment of Fe and Ni at metal and oxide grain boundaries in corroded zircaloy-2, Corros. Sci. 65 (2012) 10–12 https://doi.org/10.1016/j.corsci.2012.08.061 .

[28] G. Kresse, J. Hafner, Ab initio molecular dynamics for liquid metals, Phys. Rev. B 47 (1) (1993) 558–561 https://doi.org/10.1103/PhysRevB.47.558 .

[29] G. Kresse, J. Hafner, Ab initio molecular-dynamics simulation of the liquid-metal−amorphous-semiconductor transition in germanium, Phys. Rev. B 49 (20) (1994) 14251–14269 https://doi.org/10.1103/PhysRevB.49.14251 .

[30] G. Kresse, J. Furthmüller, Efficiency of ab-initio total energy calculations for metals and semiconductors using a plane-wave basis set, Comput. Mater. Sci. 6 (1) (1996) 15–50 https://doi.org/10.1016/0927-0256(96)00008-0 .

[31] J.P. Perdew, K. Burke, M Ernzerhof, Generalized gradient approximation made simple, Phys. Rev. Lett. 77 (18) (1996) 3865–3868 https://doi.org/10.1103/PhysRevLett.77.3865 .

[32] J.P. Perdew, K. Burke, M Ernzerhof, Generalized gradient approximation made simple [Phys. Rev. Lett. 77, 3865 (1996)], Phys. Rev. Lett. 78 (7) (1997) 1396−1396 https://doi.org/10.1103/PhysRevLett.78.1396 .

[33] M. Youssef, B. Yildiz, Intrinsic point-defect equilibria in tetragonal ZrO{}_{2}$: density functional theory analysis with finite-temperature effects, Phys. Rev. B 86 (14) (2012) 144109 https://doi.org/10.1103/PhysRevB.86.144109 .

[34] Zhao, Z.Redox kinetics study for chemical-looping combustion, water and co splitting using nickel and cerium-based oxygen carrier, Massachusetts Institute of Technology, 2012.

[35] H.P. Beck, C. Kaliba, On the solubility of Fe, Cr and Nb in ZrO2 and its effect on thermal dilatation and polymorphic transition, Mater. Res. Bull. 25 (9) (1990) 1161–1168 https://doi.org/10.1016/0025-5408(90)90146-S .

[36] R. Ruh, H.J. Garrett, Reactions of zirconia and chromium, J. Am. Ceram. Soc. 47 (12) (1964) 627–629 https://doi.org/10.1111/j.1151-2916.1964.tb13121.x .

[37] Sponchia, G.Zirconia advanced ceramic materials for functional and structural applications, Universita Ca'Foscari Venezia, 2016.

[38] A.K. Bhattacharya, V. Shklover, W. Steurer, G. Witz, H. Bossmann, O. Fabrichnaya, Ta2O5−Y2O3−ZrO2 system: experimental study and preliminary thermodynamic description, J. Eur. Ceram. Soc. 31 (3) (2011) 249–257 https://doi.org/10.1016/j.jeurceramsoc.2010.09.009 .

[39] A. Kumar, D. Rajdev, D.L. Douglass, Effect of oxide defect structure on the electrical properties of ZrO2, J. Am. Ceram. Soc. 55 (9) (1972) 439–445 https://doi.org/10.1111/j.1151-2916.1972.tb11336.x .

[40] R.W. Vest, N.M. Tallan, W.C. TRIPP, Electrical Properties and Defect Structure of Zirconia: I, Monoclinic Phase, J. Am. Ceram. Soc. 47 (12) (1964) 635–640 https://doi.org/10.1111/j.1151-2916.1964.tb13124.x .

[41] H. Muta, Y. Etoh, Y. Ohishi, K. Kurosaki, S. Yamanaka, Ab initio study of hydrogen diffusion in zirconium oxide, J. Nucl. Sci. Technol. 49 (5) (2012) 544–550 https://doi.org/10.1080/00223131.2012.676820 .

[42] K. Une, K. Sakamoto, M. Aomi, J. Matsunaga, Y. Etoh, I. Takagi, S. Miyamura, T. Kobayashi, K. Ito, P. Barberis, S.W. Dean, Hydrogen absorption mechanism of zirconium alloys based on characterization of oxide layer, J. ASTM Int. 8 (5) (2011) 102950 https://doi.org/10.1520/JAI102950 .

[43] D.L. Douglass, C. Wagner, The oxidation of oxygen-deficient zirconia and, J. Electrochem. Soc. 113 (7) (1966) 6.

[44] T. KOBAYASHI, T. SASAKI, I. TAKAGI, H. MORIYAMA, Solubility of Zirconium(IV) Hydrous Oxides, J. Nucl. Sci. Technol. 44 (1) (2007) 90–94 https://doi.org/10.1080/18811248.2007.9711260 .

[45] S.Ø. Stub, E. Vøllestad, T. Norby, Mechanisms of Protonic Surface Transport in Porous Oxides: example of YSZ, J. Phys. Chem. C 121 (23) (2017) 12817–12825 https://doi.org/10.1021/acs.jpcc.7b03005 .

[46] L. Chen, J. Hu, R.M. Richards, Catalytic properties of nanoscale iron-doped zirconia solid-solution aerogels, ChemPhysChem 9 (7) (2008) 1069–1078 https://doi.org/10.1002/cphc.200800041 .

[47] B. Samaranch, P. Ramírez de la Piscina, G. Clet, M. Houalla, P. Gélin, N. Homs, synthesis and characterization of Ta2O5−ZrO2 systems: structure, surface acidity, and catalytic properties, Chem. Mater. 19 (6) (2007) 1445–1451 https://doi.org/10.1021/cm062704z .

The role of doping and microstructure on hydrogen solubility in monoclinic ZrO$_2$:
Experimental validations of simulated defect chemistry

William J. Bowman, Jing Yang & Bilge Yildiz

Laboratory for Electrochemical Interfaces

Department of Nuclear Science and Engineering

Department of Materials Science and Engineering

Massachusetts Institute of Technology

77 Massachusetts Avenue, Cambridge, Massachusetts, USA 02139
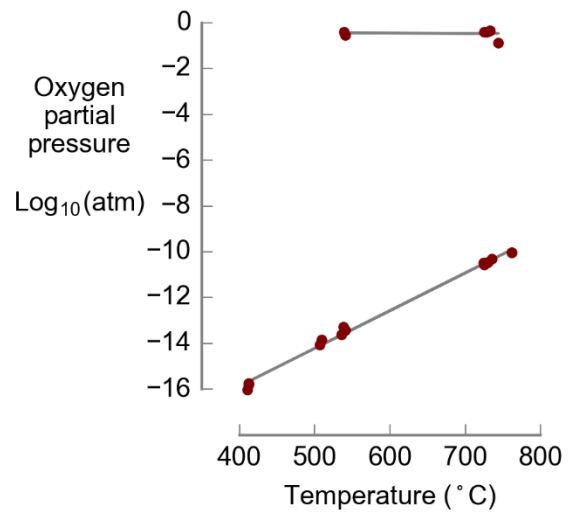
Supporting Information

Figure S1. The oxygen partial pressure was measured under each hydrating gas using a Nernst cell.

Figure S2. Hydrating the Cr-doped ZrO_2 caused a reversible color change from dark green-blue before hydration (left) to lighter green-blue after hydration (right).
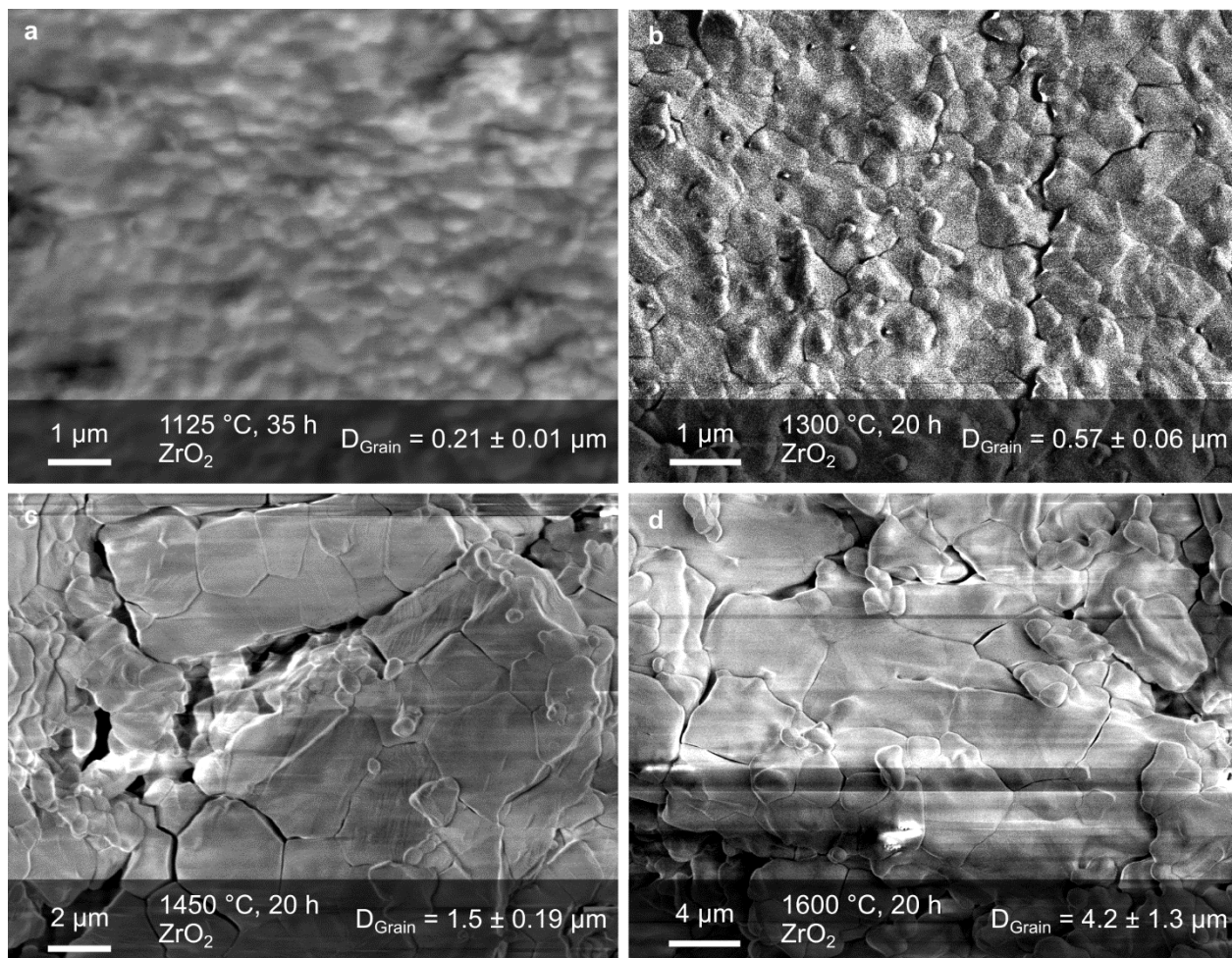
Figure S3. SEM images showing that annealing of ZrO_2 increased the grain size; the mean grain size and one standard deviation are provided.
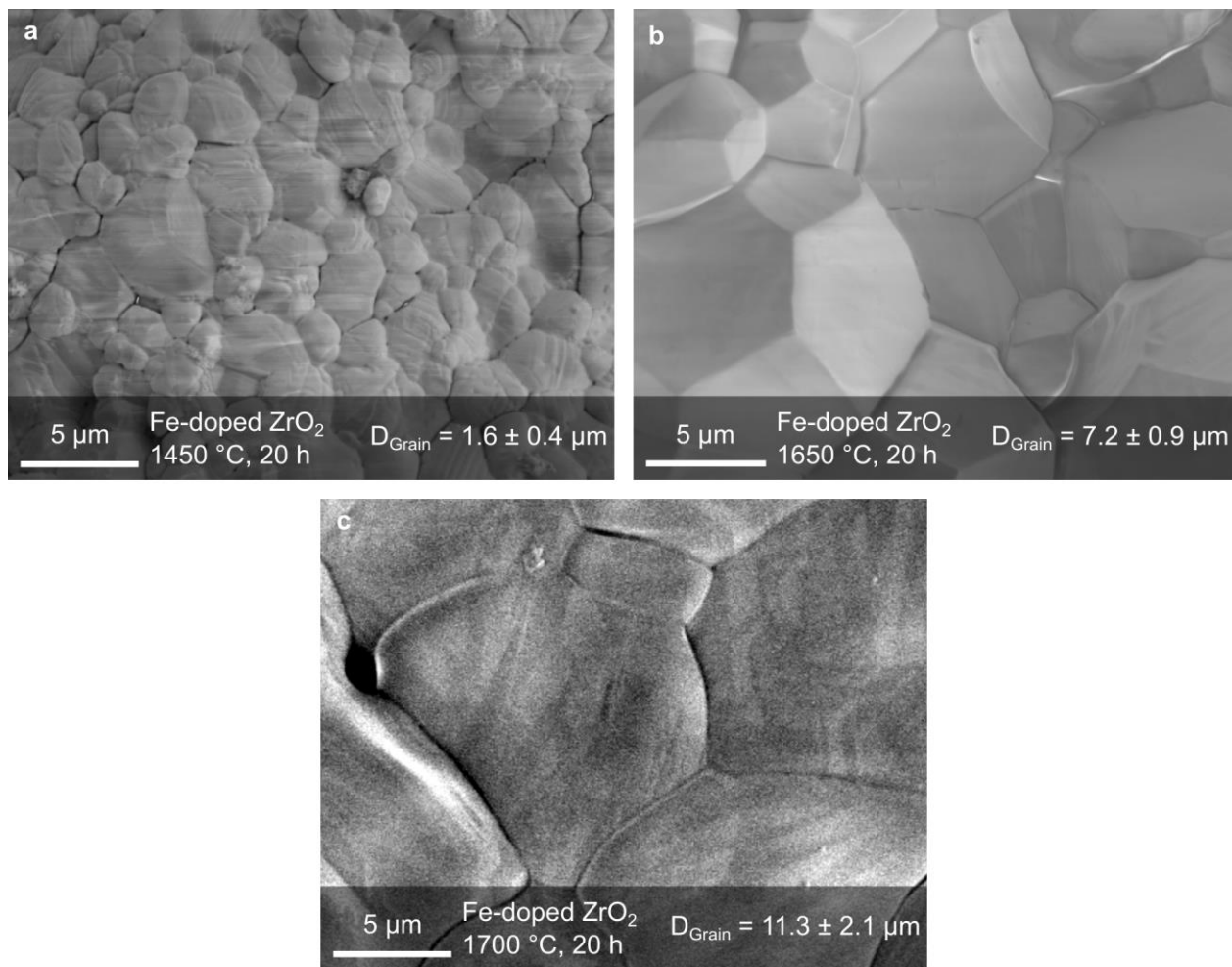
Figure S4. SEM images showing that annealing of Fe-doped ZrO$_2$ increased the grain size.
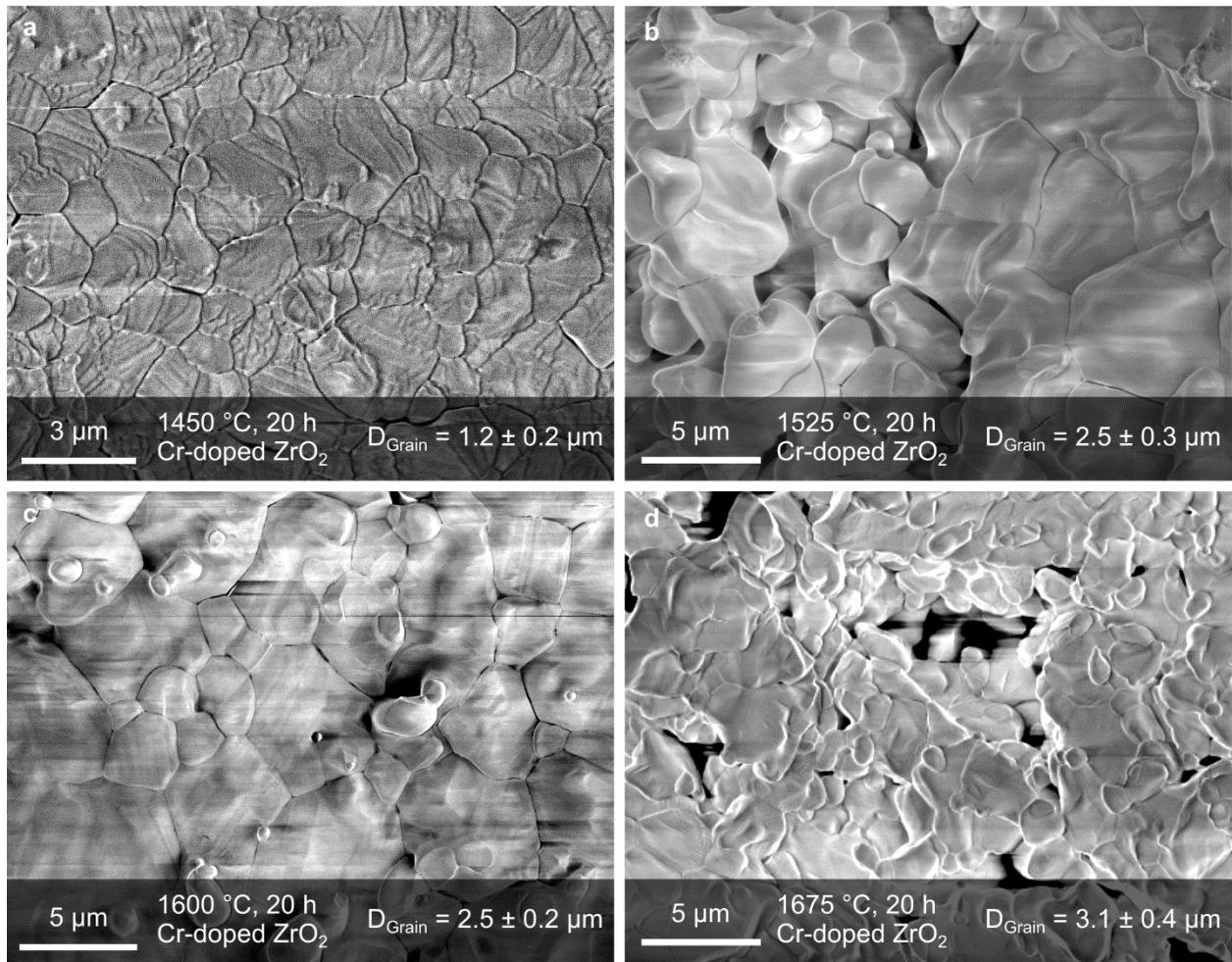
Figure S5. SEM images showing that annealing of Cr-doped ZrO_2 increased the grain size.
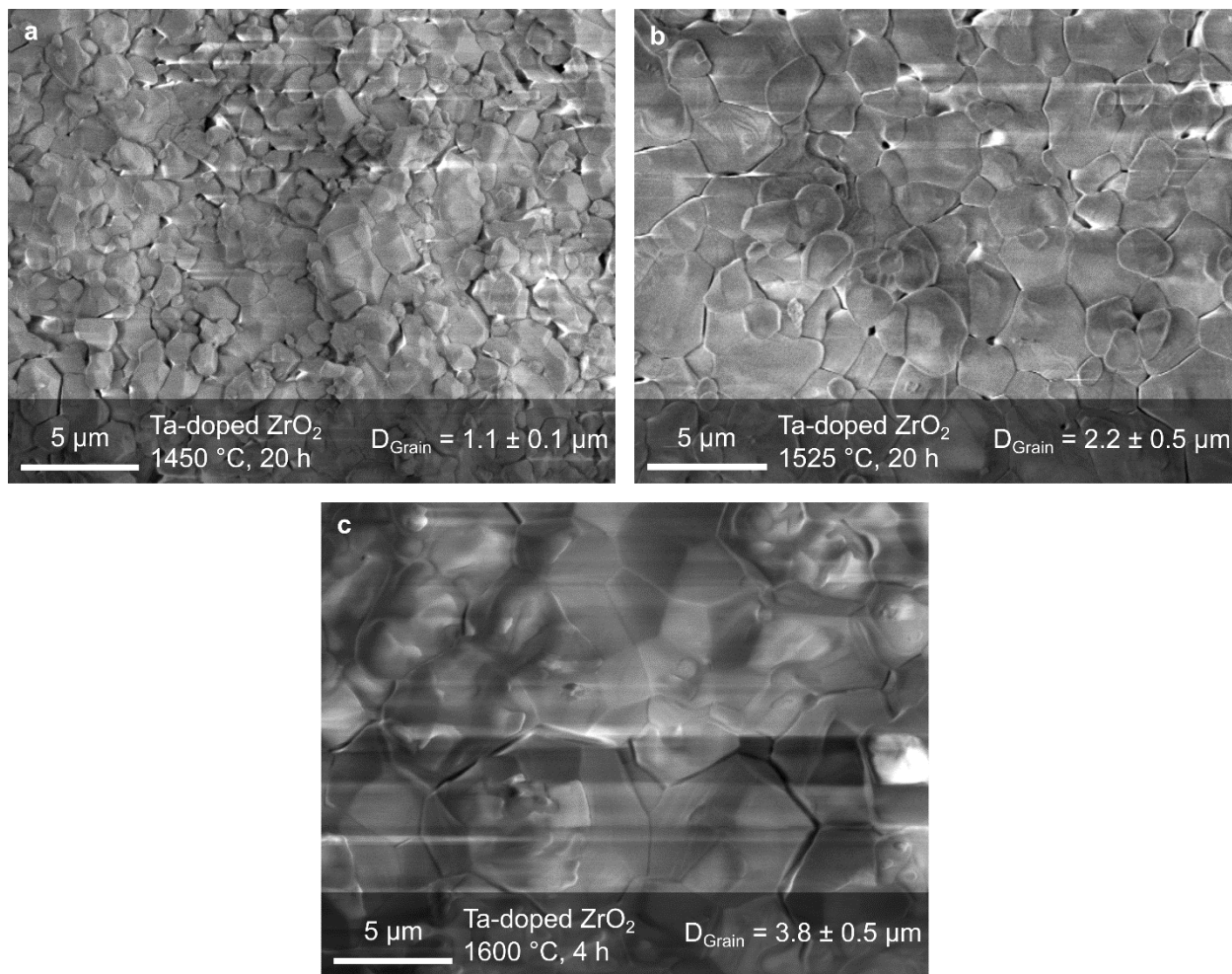
Figure S6. SEM images showing that annealing of Ta-doped ZrO_2 increased the grain size.
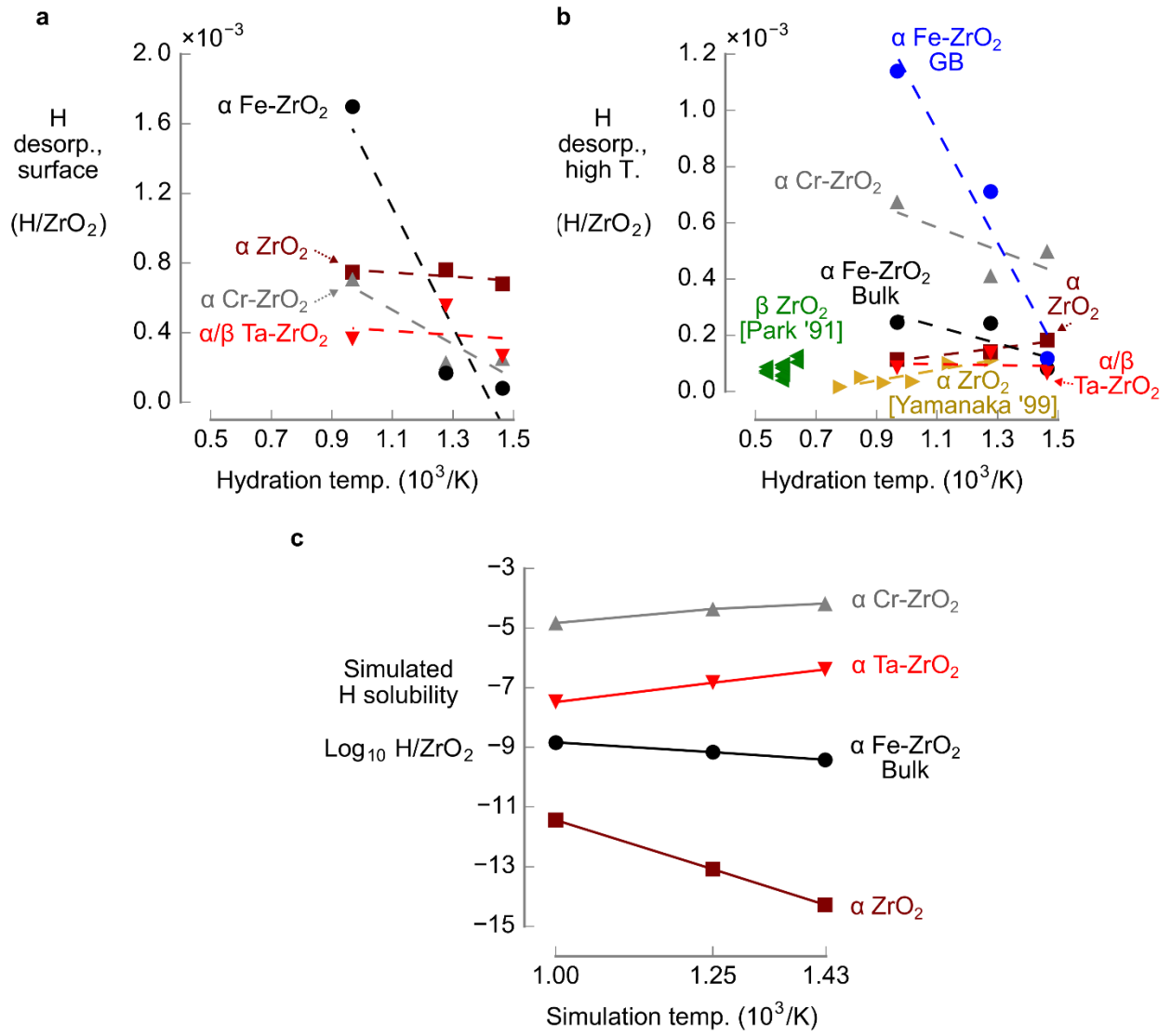
Figure S7. Solubility measurements and simulations from Figure 8 replotted with linear and log$_{10}$ scale, respectively.

Table S1. The concentrations of impurities in the as-purchased ZrO_2 precursor powder (99.978 % purity; Alpha Aesar, Puratronic) was measured by the vendor using inductively-coupled plasma mass spectrometry.

Impurity	Si	Hf	Ca	Fe	K	Mg	Sr
Concentration (ppm)	73	30	27	14	4	3	1

Table S2. Grain size was measured as a function of sintering temperature using SEM images. Samples were sintered in alumina crucibles open to air for 20 h with heating and cooling rates of 150 °C/hr.

	Sintering temperature (°C)							
	1125	1300	1450	1525	1600	1650	1675	1700
ZrO_2	0.21 ± 0.01	0.57 ± 0.06	1.5 ± 0.19		4.2 ± 1.3			
Fe-doped			1.63 ± 0.38			7.21 ± 0.91		11.3 ± 2.18
Cr-doped			1.24 ± 0.18	2.54 ± 0.33	2.53 ± 0.23		3.09 ± 0.36	
Ta-doped			1.07 ± 0.11	2.19 ± 0.48	3.28 ± 0.52			

Table S3. Integration windows used to quantify H desorption from water release rate. Determined from annealing-temperature-dependent desorption measurements

Sample	Annealing temp. (°C)	Hydration temp. (°C)	Temperature range of integration (°C)		
			Peak 1	Peak 2	Peak 3
ZrO$_2$	1125	410	50 – 450	450 – 1000	
	1125	510	50 – 450	450 – 1000	
	1125	760	50 – 450	450 – 1000	
	1300	760	50 – 500	500 – 1000	
	1450	760	50 – 450	450 – 1000	
	1600	760	50 – 450	450 – 1000	
Cr-doped ZrO$_2$	1450	410	50 – 300	300 – 1000	
	1450	510	50 – 350	350 – 1000	
	1450	760	50 – 350	350 – 1000	
	1525	760	50 – 350	350 – 1000	
	1600	760	50 – 350	350 – 1000	
	1675	760	50 – 350	350 – 1000	
Fe-doped ZrO$_2$	1450	410	50 – 250	250 – 450	450 – 1000
	1450	510	50 – 250	250 – 500	500 – 1000
	1450	760	50 – 250	250 – 480	480 – 1000
	1650	760	50 – 250	250 – 550	550 – 1000
	1700	760	50 – 250	250 – 600	600 – 1000
Ta-doped ZrO$_2$	1450	410	50 – 450	450 – 1000	
	1450	510	50 – 450	450 – 1000	
	1450	760	50 – 450	450 – 1000	
	1525	760	50 – 450	450 – 1000	
	1600	760	50 – 450	450 – 1000	

References

(1)   Balaji Gopal, C.; M. Haile, S. An Electrical Conductivity Relaxation Study of Oxygen Transport in Samarium Doped Ceria. *J. Mater. Chem. A* **2014**, *2* (7), 2405–2417. https://doi.org/10.1039/C3TA13404K.

(2)   Khatamian, D.; Manchester, F. D. An Ion Beam Study of Hydrogen Diffusion in Oxides of Zr and Zr-Nb (2.5 Wt%). *J. Nucl. Mater.* **1989**, *166*, 300–306.

(3)   Kumar, A.; Rajdev, D.; Douglass, D. L. Effect of Oxide Defect Structure on the Electrical Properties of ZrO2. *J. Am. Ceram. Soc.* **1972**, *55* (9), 439–445. https://doi.org/10.1111/j.1151-2916.1972.tb11336.x.

(4)   Sinhamahapatra, A.; Jeon, J.-P.; Kang, J.; Han, B.; Yu, J.-S. Oxygen-Deficient Zirconia (ZrO_{2-x}): A New Material for Solar Light Absorption. *Sci. Rep.* **2016**, *6* (1). https://doi.org/10.1038/srep27218.

(5)   Youssef, M.; Yang, M.; Yildiz, B. Doping in the Valley of Hydrogen Solubility: A Route to Designing Hydrogen-Resistant Zirconium Alloys. *Phys. Rev. Appl.* **2016**, *5* (1). https://doi.org/10.1103/PhysRevApplied.5.014008.